Nanoscale

PAPER

Published on 26 September 2019
Licence and permissions

Check for updates

Cite this: *Nanoscale*, 2019, **11**, 18449

Raman and electrical transport properties of few-layered arsenic-doped black phosphorus†

Nihar R. Pradhan,[a,b]* Carlos Garcia,[b,c] Michael C. Lucking,[d] Srimanta Pakhira,[b,e,f,g] Juan Martinez,[b,c] Daniel Rosenmann,[h] Ralu Divan,[h] Anirudha V. Sumant,[h] Humberto Terrones,[d] Jose L. Mendoza-Cortes,[b,c,g] Stephen A. McGill,[b] Nikolai D. Zhigadlo[i,j] and Luis Balicas[b,c]*

Received 29th May 2019,
Accepted 24th September 2019

DOI: 10.1039/c9nr04598h

rsc.li/nanoscale

Black phosphorus (b-P) is an allotrope of phosphorus whose properties have attracted great attention. In contrast to other 2D compounds, or pristine b-P, the properties of b-P alloys have yet to be explored. In this report, we present a detailed study on the Raman spectra and on the temperature dependence of the electrical transport properties of As-doped black phosphorus (b-AsP) for an As fraction x = 0.25. The observed complex Raman spectra were interpreted with the support of Density Functional Theory (DFT) calculations since each original mode splits in three due to P–P, P–As, and As–As bonds. Field-effect transistors (FET) fabricated from few-layered b-AsP exfoliated onto Si/SiO_2 substrates exhibit hole-doped like conduction with a room temperature ON/OFF current ratio of ~10^3 and an intrinsic field-effect mobility approaching ~300 cm^2 V^{-1} s^{-1} at 300 K which increases up to 600 cm^2 V^{-1} s^{-1} at 100 K when measured *via* a 4-terminal method. Remarkably, these values are comparable to, or higher, than those initially reported for pristine b-P, indicating that this level of As doping is not detrimental to its transport properties. The ON to OFF current ratio is observed to increase up to 10^5 at 4 K. At high gate voltages b-AsP displays metallic behavior with the resistivity decreasing with decreasing temperature and saturating below T ~100 K, indicating a gate-induced insulator to metal transition. Similarly to pristine b-P, its transport properties reveal a high anisotropy between armchair (AC) and zig-zag (ZZ) directions. Electronic band structure computed through periodic dispersion-corrected hybrid Density Functional Theory (DFT) indicate close proximity between the Fermi level and the top of the valence band(s) thus explaining its hole doped character. Our study shows that b-AsP has potential for optoelectronics applications that benefit from its anisotropic character and the ability to tune its band gap as a function of the number of layers and As content.

Introduction

The quest for new materials with unique properties and technological potential is increasing rapidly due to the belief that our current technology is approaching the limit of miniaturization of metal–oxide semiconductor FETs.[1] Two-dimensional semiconductors are being explored as materials that could be integrated with current silicon technology to perform specific functions as hardware enhancers or as materials meeting the criteria set by the International Technology Roadmap for Semiconductors.[2] Among these materials, Black phosphorus (b-P) has attracted great interest due to its unique physical properties,[3] such as a layer-dependent direct band gap ranging from 0.3 to 2.0 eV (ref. 4, 5 and 6) and high room-temperature

[a]Department of Chemistry, Physics and Atmospheric Sciences, Jackson State University, Jackson, MS 39217, USA. E-mail: nihar.r.pradhan@jsums.edu
[b]National High Magnetic Field Laboratory, Florida State University, Tallahassee, FL 32310, USA. E-mail: balicas@magnet.fsu.edu
[c]Department of Physics, College of Arts and Sciences, Florida State University, Tallahassee, Florida, 32306, USA
[d]Department of Physics, Applied Physics and Astronomy, Rensselaer Polytechnic Institute, Troy, New York 12180, USA
[e]Discipline of Physics and Metallurgy Engineering & Materials Science, Indian Institute of Technology Indore (IITI), Simrol, Khandwa Road, Indore, 453552 MP, India
[f]Department of Chemical & Biomedical Engineering, FAMU-FSU College of Engineering, Florida State University, Tallahassee, Florida, 32310, USA
[g]Department of Scientific Computing, Materials Science and Engineering, High Performance Materials Institute, Florida State University, Tallahassee, Florida, 32304, USA
[h]Center for Nanoscale Materials, Argonne National Laboratory, 9700 S-Cass Avenue, Argonne, IL-60439, USA
[i]Department of Chemistry and Biochemistry, University of Bern, Freiestrasse 3, CH-3012 Bern, Switzerland
[j]CrystMat Company, CH-8046 Zurich, Switzerland

† Electronic supplementary information (ESI) available. See DOI: 10.1039/c9nr04598h

This journal is © The Royal Society of Chemistry 2019

hole mobilities in excess of 10^3 cm^2 V^{-1} s^{-1} (ref. 7 and 8). The direct band gaps also depend upon the stacking order of the layers.[6] Phosphorene nanoribbons produced along zig-zag and arm-chair direction shows interesting electronic properties.[9] The nature of direct band gap of b-P makes them ideal candidates for photovoltaic applications.[10,11] These properties suggest that b-P is not only attractive for electronic, photovoltaic, and optoelectronic applications[6–14] but also suitable for the development of batteries, supercapacitors, and for biomedical applications.[15–17]

The band gap tunability of b-P opens unique possibilities for the development of broadband photodetectors that could work from the visible all the way to the IR spectral range, when combined with transition metal dichalcogenides in a heterostructure. Previous reports already demonstrated that a transistor based on pristine b-P exhibits an ON to OFF current ratio ranging from ~10^2 to ~10^5 and mobilities as high as 300 cm^2 V^{-1} s^{-1} when fabricated on a SiO_2 substrate.[5,18–20] However, one of the obstacles for fabricating high quality b-P devices is its quick degradation when exposed to environmental conditions. Moisture degrades the quality of the crystal significantly, making it difficult to fabricate devices that maintain its intrinsic properties over time. Attempts have been made to preserve the pristine nature of b-P by encapsulating it under inert atmospheric conditions just after exfoliation between dielectric layers like Al_2O_3, HfO_2 or *h*-BN. In one case, a high room temperature mobility up to ~1000 cm^2 V^{-1} s^{-1} was reported when encapsulated between *h*-BN layers.[21] In fact, quantum hall-effect was already reported from few layered b-P FETs encapsulated in *h*-BN.[5]

In order to improve the properties of b-P, the doping of a few chemical elements such as potassium (K), arsenic (As), selenium (Se), and tellurium (Te) was demonstrated through different methods.[22–28] For instance, K atoms were sprinkled on top of the b-P crystals by means of an *in situ* surface doping technique, converting it from a semiconductor to a band-inverted semimetal.[22] Tunable and precise fractions of As were incorporated into BP crystals through a chemical vapor transport (CVT) technique without suppressing its semiconducting response but tuning its electronic and optical properties.[25] Se atoms were also incorporated into b-P *via* the CVT method[26] improving its optoelectronic response when used as a photodetector; the external quantum efficiency increased from 149% to 2993% leading to a concomitant increase in the photoresponsivity from 0.77 A/W to 15.33 A/W, which represents a 20-fold increase with respect to undoped BP. Te, at a level of 0.1% atomic ratio, was also incorporated into BP through a high-pressure method[24] boosting its room-temperature field-effect hole mobility up to 1850 cm^2 V^{-1} s^{-1} and improving its stability under ambient conditions (room-temperature hole mobilities >200 V^{-1} s^{-1} after 21 days). However, in b-P based field-effect transistors Te doping also led to a large distribution in hole mobilities and ON/OFF current ratios.[28] More recently, higher levels of uniform Te incorporation was achieved through a CVT method.[29] Notice that the different synthetic routes, *e.g.* high pressure conversion or CVT growth, to produce b-P introduce or retain the different metallic impurities present, for example, in the precursors[30] implying that this material is, to a certain degree, always alloyed.

Here, we study the physical properties of As-doped black phosphorus (b-AsP) (for the synthesis see Methods section) and compare the observed results with those reported for pristine black phosphorus. As mentioned above, non-isoelectronic substitution to form b-P alloys has been explored in ref. 31 and 32 finding that the different dopants have a significant effect on the mobilities and band gaps of the synthesized powders. However isoelectronic substitution to form sizeable single crystals has not yet been intensively explored. Therefore, a primary goal of alloying black phosphorus with As is to form stable large single-crystals over a broad range of dopings that have tunable band gaps particularly below 0.3 eV (4.13 μm) or approaching 0.1 eV with no mid-gap impurity states. Such high quality alloys would allow us to cover a broad spectral range, or wavelengths from 5 to 10 μm, where optoelectronic applications focused on the infrared range and based on 2D materials, such as high performance thermal imaging, have yet to be developed. In addition, as discussed below, As tends to form clusters, making it possible that a particular As concentration and its related As clustering could increase the anisotropy in its transport properties and this could be used to produce unique devices.[33] Smaller gaps make it possible to easily tune, *via* a gate voltage, the transport properties of b-AsP towards a metallic regime and perhaps even to a superconducting state at ambient pressure.

We were able to synthesize layered b-AsP with different compositions (b-As_xP_{1-x}, with x ranging from 0 to 0.4), *via* a high-pressure and high-temperature technique, using a cubic-anvil, (see ESI, Fig. S1, Table S1, and Fig. S2,† for X-ray diffraction, its analysis, and Energy Dispersive Spectroscopy, respectively). A similar high pressure synthesis route was previously used in ref. 25 and 34 to synthesize b-P and b-As_xP_{1-x} (x = 0.05, 0.1) with the goal of studying their bulk superconducting properties under very high pressures. More recently, b-AsP was synthesized over a broad range of compositions by Liu *et al.*[25] through a mineralizer-assisted chemical transport reaction initially used in ref. 24 to study the stability of AsP alloys finding, through infrared absorption, that the band gap decreases sharply as a function of the As concentration until the As fraction reaches x = 0.25 beyond which the gap (of ~175 meV) becomes very weakly depend on x. Therefore, in this manuscript we focus on the physical properties of x = 0.25 that provide an approximate assessment on those alloys characterized by higher values of x. Although, according to ref. 35, which studied the b-AsP composition and its plausible atomic configurations, some particular As and P arrangements could lead to dramatic enhancements in carrier mobilities, that is by nearly one order magnitude with respect to b-P. One of our goals is to explore how the particular As arrangement observed in b-$As_{0.25}P_{0.75}$ could affect its carrier mobilities relative to b-P. Therefore, in contrast to ref. 25, here we explore in detail its anisotropic transport properties as a function of temperature, the Schottky barriers as function of gate voltage

 This journal is © The Royal Society of Chemistry 2019

with both measurements indicating that this system becomes metallic upon gating, and study its polarization dependent Raman scattering. Although a detailed characterization as a function x is laudable, it is beyond the scope of this manuscript and will be reported elsewhere. After synthesizing the b-AsP crystals, we used X-ray diffraction to confirm that our b-AsP crystals crystallize in the orthorhombic structure of pristine b-P with strong planar covalent bonding and weak interlayer coupling between layers, see ESI.† This structure was used for our computational analysis in order to calculate the band structure of b-AsP, as well as the electronic bands of trilayers, bilayers, and monolayer b-AsP in order to contrast with our experimental results.

Experimental methods

Raman measurements

The Raman measurements of few layered As-bP crystals were performed on a home-built optical microscope using a narrow linewidth 532 nm laser. A small camera and incandescent lamp were used to view the sample and to align the laser excitation prior to the measurement. The excitation spot size on the sample was approximately 3 μm in diameter, measured by using pre-patterned grids and a 60× objective lens. The microscope permitted user control of the intensity and polarization of the laser excitation. The backscattering geometry was used for collection. Signal analysis was done using a 500 mm focal length spectrometer equipped with a 1200 g mm^{-1} grating. A Princeton Instruments liquid nitrogen-cooled research-grade CCD was used to detect the Raman peaks. The Raman spectra on the polymer-coated sample were performed after a month of keeping in oxygen environment using a Renishaw inVia Raman setup.

Device fabrication and measurements

Few layers of As-bP crystals were mechanically exfoliated using blue Nitto tape (product # SPV 224PR-M) and then transferred onto a clean 285 nm thick SiO_2 layer. Electrical contacts were patterned using standard e-beam lithography techniques. Metal contacts were deposited *via* e-beam evaporation at 10^{-7} Torr pressure, and consisted of 80 nm of Au on top of a 5 nm layer of Ti. After deposition, acetone was used in a lift off procedure to remove the unwanted PMMA resist. The devices were vacuum annealed at 120 °C for ~20 h, and immediately coated with a ~20 nm thick Cytop™ (amorphous fluoropolymer) layer to prevent air exposure. Electrical measurements were conducted using a combination of dual channel source meters, Keithley 2400, Keithley 2612B and Keithley 2635, coupled to a Quantum Design Physical Property Measurement System.

Theoretical method

Raman mode calculations using DFT. The Raman calculations were performed using the plane wave code Quantum Espresso[36] under the local density approximation (LDA) with norm conserving pseudopotentials and a plane wave basis up to an energy cutoff of 1360 eV. The lattice constants and atomic positions were fully relaxed with a force convergence threshold of 0.00025 eV $Å^{-1}$. The Brillouin zone was sampled with a 22 × 16 Monkhorst–Pack k-point grid. Density functional perturbation theory (DFPT) with linear response was used to calculate the vibrational modes at the gamma point. The Raman coefficients were obtained from the second order response with respect to an electric field.[37] Several monolayer models were considered for the arsenic doped black phosphorous depending on the arsenic concentration. One, two, and three phosphorous atoms were replaced with arsenic atoms in the unit cell for the 25%, 50%, and 75% arsenic doping, respectively. For the 50% case, there are three distinct ways to arrange the atoms in the unit cell. All three were calculated and the Raman intensities are superimposed. A 2 × 2 supercell was used to simulate a 62.5% arsenic doping concentration and a 25% doping configuration in which As atoms were clustered instead of uniformly dispersed.

Band gap calculations *via* hybrid DFT. Periodic hybrid density functional theory (DFT)[38] was employed to perform all the computations as implemented in the *ab initio* CRYSTAL14 suite code, which makes use of localized (Gaussian) basis sets.[39] Dispersion effects (DFT-D) were included in the form of semi-empirical Grimme's (-D2) dispersion corrections. Thus, unrestricted DFT dispersion corrected hybrid UDFT-HSE06-D2 (or HSE06-D for short) method was used. The HSE06-D approach incorporates van der Waals (vdW) dispersion interactions in the As-doped black phosphorous systems.[40–43] DFT-D has been shown to give quite accurate thermochemistry for both covalently bonded systems and systems dominated by dispersion forces.[41–44] The geometries of the pristine bulk structure *i.e.* crystal structures of As-doped black phosphorous ($As_{0.25}BP$), that is three layers (3L), two layers (2L) and monolayer (1L) were optimized using the HSE06-D method.[38] Note that this code (CRYSTAL14) performs the calculations based on Gaussian basis sets and not on plane waves.[39] Here, triple-zeta valence with polarization quality (TZVP) Gaussian basis sets were used for As and P atoms.[45] The threshold used for evaluating the convergence of the energy, forces, and electron density was set at 10^{-7} a.u. for each parameter. The DFT-D (here HSE06-D) method was used for geometry optimization because densities and energies obtained with the method are less affected by spin contamination than other approaches.[46–48] After obtaining the optimized bulk crystal structure, three layers (3L), two layers (2L) and monolayer (1L) b-AsP, the electronic properties (*i.e.* band structures) for all these materials were calculated with the same UHSE06-D method. Integrations inside of the first Brillouin zone were sampled on 15 × 15 × 15 and 20 × 20 × 1 Monkhorst–Pack[49] k-mesh grids for the bulk crystalline structure and the 2D layered structures of b-AsP, respectively, to calculate both the geometry optimization and the electronic properties. The reciprocal space for all the structures was sampled by a Γ-centered Monkhorst–Pack scheme with a resolution of around $2\pi \times 1/60$ $Å^{-1}$. The band pathway followed the symmetry points: Z–T–Y–Γ–X–L–Z–Γ for bulk crystal structure of the

b-AsP material and Γ–Y–S–X–Γ for the 2D layered structures (*i.e.* monolayer, 2L and 3L). The conventional unit cells for the 2D monolayer, 2L and 3L b-AsP have a 2D characteristic in the x and y directions. The z direction, on the other hand, is treated within a vacuum by employing a ~500 Å length for the z-axis to accommodate the vacuum environment. The VESTA, a visualization code, was used to create the graphics and analysis of the crystal structures for all the systems studied here.[50]

Results and discussion

The objective of this study on few-layered As-doped bP is to elucidate its detailed electrical transport and Raman properties, which have yet to be reported.[25] The b-AsP crystals are very sensitive to environmental conditions just like pristine b-P crystals.[20,21,51,52] Few-layered b-AsP crystals were exfoliated using the micromechanical exfoliation technique inside an Ar-filled glove box to protect it from oxidation and concomitant degradation and subsequently transferred onto clean Si/SiO_2 substrates. Initially, we checked the sensitivity of few-layered flakes to air exposure by monitoring their degradation under an optical microscope at room temperature (see ESI Fig. S3†). We did not find any clear sign of degradation for thin b-AsP crystals exposed to air for 1 hour. After exfoliation and transfer of the b-AsP crystals onto SiO_2 substrates within the Ar glove box, we located the thinnest flakes with an optical microscope and spin-coated these with PMMA photoresist thus subjecting them to a few minutes of air exposure. We checked the crystal thicknesses *via* an AFM and by comparing the color of these flakes with the color of those observed under optical microscopy. We estimate the thickness of the flakes used for the electrical transport characterization and for the Raman study to be ~7–10 nm thick, corresponding to 12–14 atomic layers of b-AsP. Raman and polarization dependent Raman measurements were conducted on flakes composed of a few atomic layers after covering them with a 30 nm thick protective layer of Cytop™, which is transparent to light (see, Fig. S4 in ESI†). We found that the b-AsP crystals remain chemically stable for a much longer period when coated with Cytop™ or PMMA (Fig. S4d in ESI†) when compared to uncoated crystals. For example, the Raman data collected on polymer-encapsulated flakes after longer time remains nearly identical to the Raman spectra collected immediately after exfoliation (ESI Fig. S4d†).

We performed a Raman spectroscopy study on few layered b-AsP crystals using unpolarized and polarized light from a 532 nm laser source belonging to a home-built Raman spectrometer. Fig. 1a displays the Raman spectra of thin (~4 nm) and of thick (~20 nm) samples. The laser spot size on the samples has a diameter of ~3 μm and was measured using pre-patterned grids. Our Raman measurements clearly indicate that the Raman spectra of the b-AsP sample is quite different from that of the pristine bP crystals.[53] In pristine bP samples, one observes three major peaks associated with the P–P bonds, the out-of-plane A_{1g} mode at 363 cm^{-1}, the in-plane B_{2g} peak at 440 cm^{-1}, and the in-plane A_{2g} peak at 467 cm^{-1}.[5,18,19,54,55]

In b-AsP these three main peaks are split into additional ones associated with the As–As, As–P and P–P bonds. We observed three distinct Raman branches resulting from these bonds in the Raman shift regions 200 cm^{-1}–300 cm^{-1}, 300 cm^{-1}–400 cm^{-1} and 400 cm^{-1}–470 cm^{-1}, respectively. In the ESI† we provide a table, *i.e.* Table S2,† containing all of our

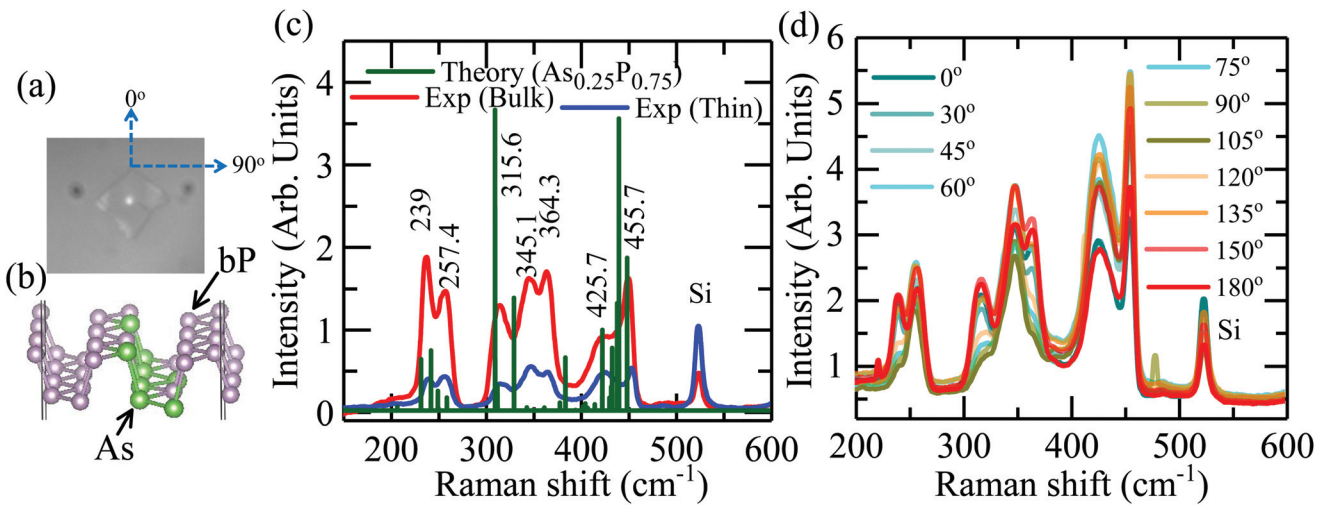

Fig. 1 (a) Optical image of the As-bP thin crystal and of the laser spot used for this Raman study. (b) Schematic of As-doped bP crystal with 25% of Arsenic (purple dots depict P atoms while green dots represent As ones). (c) Raman spectroscopy of few-layered and bulk b-$As_{0.25}P_{0.75}$ crystals. The Raman spectra contain contributions from the As–As, As–P and P–P bonds. The theoretically calculated spectrum is depicted in green color for 25% of As. (d) Polarization dependent Raman spectra of few-layered b-$As_{0.25}P_{0.75}$ crystals showing their evolution as a function of the polarization angle from 0° to 180°. An excitation laser wavelength of λ = 532 nm was used for the Raman and polarization dependent Raman measurements with a laser spot size of ~3 μm.

 This journal is © The Royal Society of Chemistry 2019

calculated Raman modes for b-$As_{0.25}P_{0.75}$. The important points are (i) all Raman modes involve As–As-, As–P, and P–P bonds, and all peaks observed in the Raman spectra are A modes due to the low point group symmetry of this compound. Notice that this contrasts with the conclusions and calculations in ref. 25 that attributes peaks in the range 200–300 cm^{-1} to As–As bonds in b-$As_{0.4}P_{0.6}$. In ref. 25 the Raman modes or peaks located between 200 cm^{-1} and 300 cm^{-1} (ref. 25) are poorly defined with overlapping peaks. This could be due to differences in sample quality, degradation of their samples, or the sensitivity of the apparatus used for the measurements.

The theoretical calculation of the Raman modes, which are detailed in the Methods section, was performed for b-AsP crystals also as a function of the As concentration. We observe that peaks in the 200–300 cm^{-1} range emerge as the As concentration is increased, in agreement with previous experiments (ref. 25). Meanwhile, the intensity of the peaks at 420–450 cm^{-1} decreases. This is likely due to the increased contribution from the As–As bonds. These low wavenumber modes can be reproduced at lower As concentrations if As formed clusters in black phosphorous instead of being uniformly distributed. One such configuration with 25% As that would yield the Raman modes observed by us according to our DFT calculations is shown in Fig. 1b (green colored lines). This particular cluster, or configuration of As atoms, leads to an excellent agreement with our experimental results. In addition, and according to our calculations, this configuration characterized by As clustering is more stable than the uniformly dispersed As one by 0.24 eV. The theoretically calculated Raman spectra for crystals containing 50%, 62.5% and 75% of As are presented in the ESI Fig. S4(a)–(c).†

Subsequently, we used polarization dependent Raman spectroscopy to study the role of the orientation of the molecular bonds on single crystals of b-AsP, as well as the anisotropic properties of this compound. A detailed experimental description of the polarization dependent Raman spectra is given in the Methods section. Fig. 1d displays the polarization (linear polarization) dependent Raman data collected using the same laser source (λ = 532 nm) previously employed to obtain the unpolarized Raman spectra discussed in Fig. 1c. A b-AsP crystal having a thickness of ~8–10 layers was chosen for the polarization dependent Raman study. The incident light is applied along the *c*-axis with the polarization rotating in the *a*–*b* plane of the crystal. The Raman spectra were obtained for polarization angles of 0, 30, 45, 60, 75, 90, 105, 120 and 180 degrees and are presented in Fig. 1d. Here, zero degrees correspond to an initial arbitrary direction. For all angles, we observed the same three groups of Raman peaks located between 200–300 cm^{-1}, 300–400 cm^{-1} and 400–475 cm^{-1}. The sharp Raman peaks confirm the crystalline orthorhombic structure of b-AsP. It shows that the relative peak position does not vary as a function of the polarization angle, although the relative amplitude of each peak does change significantly. The intensity of the peaks observed between 400 and 500 cm^{-1} increases from 0 to 60 degrees (maximum) as a function of the polarization angle (see polar plot of the angular dependence of the Raman intensity in ESI Fig. S5†) and then decreases again as the polarization angle continues to increase. The polarization dependence of the Raman spectra for an 83% As-doped b-P was previously reported in ref. 25 where the three peaks observed between 210 cm^{-1} and 270 cm^{-1} show a clear change in the Raman intensities as a function of the polarization angle. In contrast, the intensity of the Raman peaks observed between and 300 and 500 cm^{-1} in ref. 25 does not seem to show any polarization dependence. For our 25% As-doped sample one clearly observes the polarization dependence for all Raman modes.

Having detailed the Raman response we now focus on the transport properties of b-$As_{0.25}P_{0.75}$. Fig. 2a displays the optical image of one of our FETs built from b-AsP having six Ti/Au contacts. We fabricated multi-terminal contacts as shown in Fig. 2a for 2- and 4-terminal measurements (Fig. 2a), where source (S) and drain (D) electrodes are used for both sourcing the voltage (V_{ds}) and measuring the current (I_{ds}) in a 2-terminal configuration. In a 4-terminal configuration, the terminals S and D are used for sourcing/measuring the current (I_{ds}), and the leads V_1 and V_2 are used for sensing the voltage (V_{12}). The four-terminal method was used to evaluate the nearly intrinsic transport properties of b-AsP where one can minimize the role of the resistance of the contacts associated with the 2-terminal method. Fig. 2b shows the schematics of the device indicating the configuration of measurements. A transparent fluoropolymer, *i.e.* Cytop™[56,62] was used to cover the As-bP channel in order to protect the device from moisture and oxygen. Cytop™ repels oil and water, is chemically resistant and transparent with a refractive index equivalent to that of water, while displaying no fluorescence.

Our experience indicates that covering b-AsP with Cytop™, preserves its pristine properties for a considerably longer time. Cytop™ was coated *via* a spin coating method and allowed to dry under vacuum for several hours before performing electrical transport measurements. Fig. 2c displays the drain to source current I_{ds} as a function of the bias voltage V_{ds}, when using a 2-terminal configuration, for several values of the applied gate voltage V_{bg} ranging from 0 V to −20 V. The I_{ds} as a function of V_{ds} plot indicates ohmic-like response for the Ti : Au electrical contacts to As-bP. Fig. 2d displays the same I_{ds} as a function of V_{ds} plot when measured through a 4-terminal configuration where we observed much higher currents; nearly 4.5 times larger than the values measured through the 2-terminal one (Fig. 2d), indicating that 2-terminal measurements are dominated by the resistance of the contacts despite the nearly ohmic response. We estimated the resistance of the contacts (R_c) using the relation $(V_{2T}/I_{2T}-V_{4T}/I_{4T})/2$ that yields R_c ~100 kΩ μm under V_{bg} = 0 V and 40 kΩ μm under V_{bg} = −30 V, which is one order of magnitude higher than the values reported for black phosphorus using Ni and Pd contacts.[48,53] Therefore, the resistance of contacts ought to dominate the charge carrier mobilities extracted *via* the 2- and 4-terminal methods which are discussed below. Here, V_{2T} and V_{4T} refer to the bias voltages and I_{2T} and I_{4T} refers to the currents

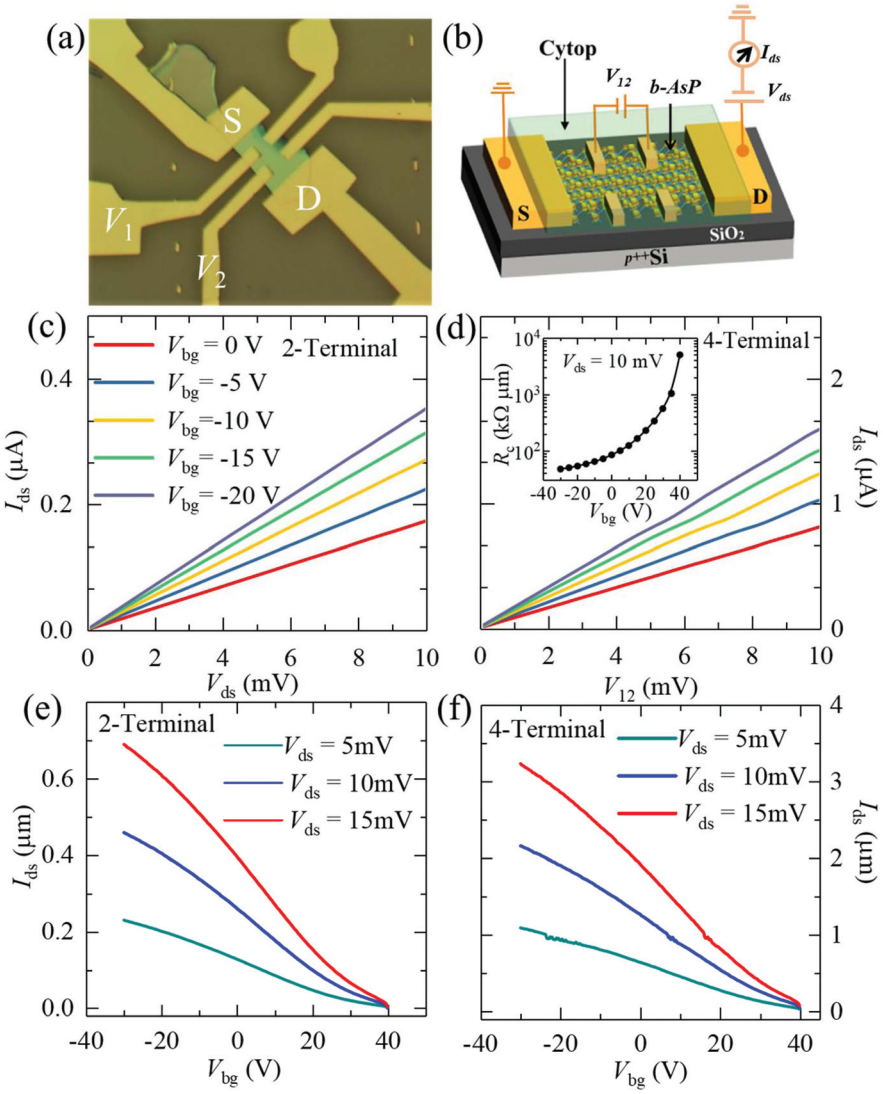

Fig. 2 (a) Optical image for one of the FETs composed of ~10 atomic layers of b-$As_{0.25}$ $P_{0.75}$ with a 70 nm of Au on a 5 nm thick layer of Ti used for the electrical contacts. The length L and width W of the channel are 10.3 μm and 5.6 μm, respectively. The length l between the two voltage contacts V_1 and V_2 is 3.8 μm. (b) Schematics of measurements. (c) Drain to source current I_{ds} as a function of the bias voltage V_{ds} measured at room temperature using a two-terminal configuration of contacts and for several applied back gate voltages V_{bg}. (d) I_{ds} as a function of V_{12} for the same sample measured with a 4-terminal configuration. Inset: Contact resistance extracted from 2- and 4-terminal measurements. (e) and (f) I_{ds} as a function V_{bg} for V_{ds} = 5 mV, 10 mV and 15 mV, in a linear scale and measured through 2- and 4-terminal configurations, respectively. These traces were collected at room temperature.

measured through 2- and 4-terminal configurations, respectively.

Fig. 2e shows the FET drain to source current I_{ds} as a function of the back gate voltage V_{bg} for fixed values of the drain to source voltage, namely V_{ds} = 5 mV, 10 mV and 15 mV, when using a 2-terminal configuration. Our few layered b-AsP FET shows hole-like conduction, while pristine b-P FET was reported to also behave as either hole-doped or to display ambipolar behavior.[5,7,11–19,57] Fig. 2f shows I_{ds} as a function of V_{bg} for the sample measured through the 4-terminal method. Notice the much larger currents extracted for the same bias voltages. As seen, our b-AsP displays hole-doped instead of ambipolar behavior due to As doping which displaces the Fermi level towards the valence band according to our band structure calculations, see ESI Fig. S6 and Table S3.† The total density of states (DOS) and the p-subshells DOS of the As are as shown in Fig. S6.† These total density of states with the contributing components of the p-subshells DOS of the As atom calculations indicate that the As-doping in bP displaces the Fermi energy level (E_F) level towards the valence band maximum and makes it hole doped (Fig. S6†). This behavior may also be influenced by the band bending (Schottky barriers) at the interface with the Ti metallic contacts.[22] We measured multiple b-AsP FETs (~5 samples) with all devices showing similar, hole-doped like behavior as a function of the applied gate-voltage. Fig. 3b shows I_{ds} as a function of V_{bg}

 This journal is © The Royal Society of Chemistry 2019

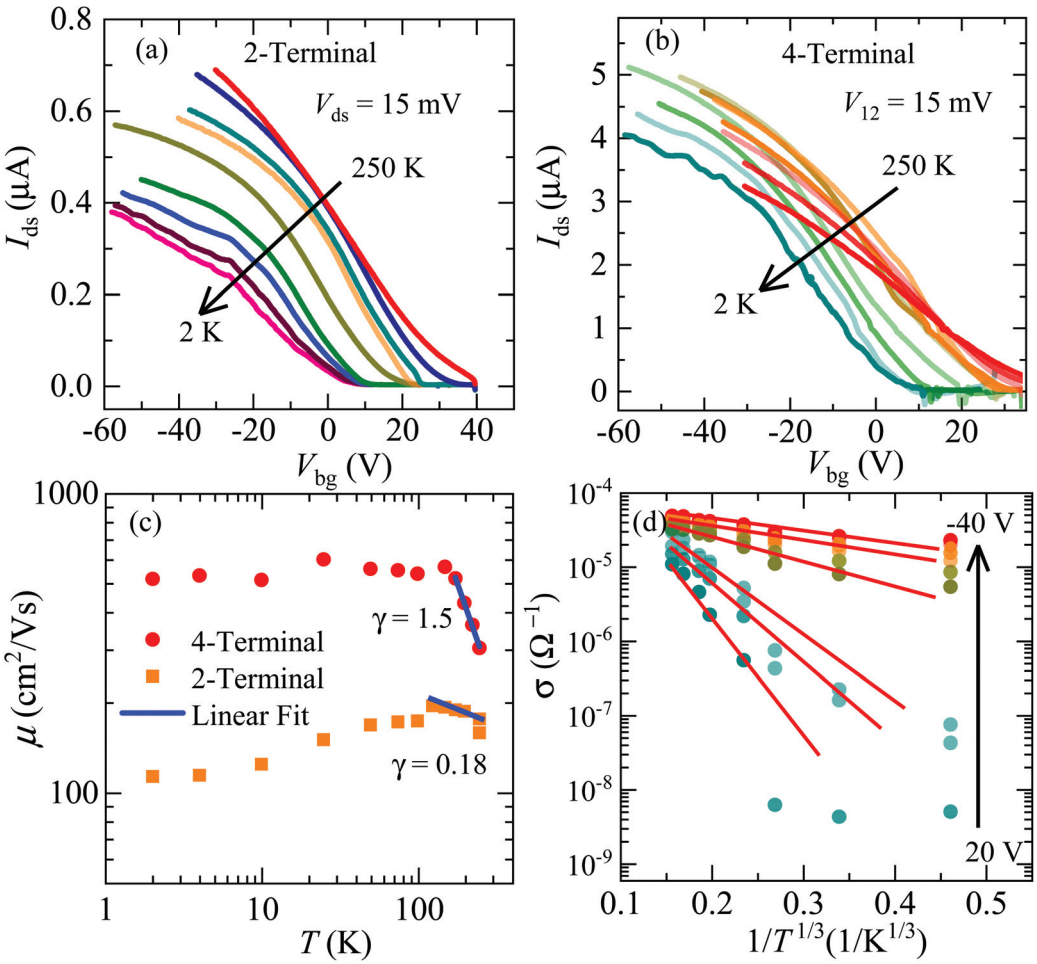

Fig. 3 (a) I_{ds} measured *via* a 2-terminal configuration under V_{ds} = 15 mV as a function of V_{bg} for several temperatures ranging from 250 K to 2 K. (b) I_{ds} as a function of V_{bg} measured through the 4-terminal method. The current extracted when using the 4-terminal method is much higher than the one collected *via* the 2-terminal one over the entire temperature range. (c) Field-effect mobilities extracted through the MOSFET transconductance formula as a function of the temperature. The 4-terminal mobility is considerably higher than the 2-terminal one indicating that the resistance of the contacts dominates the transport measured *via* the 2-terminal configuration. Solid blue lines are linear-fits to the mobility observed at high temperatures using the formula $\mu_{FE} = T^{-\gamma}$, where the exponent γ unveils the strength of the phonon scattering mechanism at higher temperatures. (d) Conductivity σ as function of $T^{-1/3}$ for several values of the gate voltage. Red lines are linear fits.

measured through a 4-terminal method. For a fixed bias voltage, the current extracted *via* the 4-terminals is considerably higher (by nearly one order of magnitude) when compared to the current measured through a 2-terminal configuration. For all measurements, the maximum channel current was limited in order to prevent damaging our FETs through the choice of small values of V_{ds}.

Pristine b-P shows exciting electrical transport properties at low temperatures such as high charge carrier mobility approaching ~6000 cm^2 V^{-1} s^{-1} below 20 K, or integer quantum Hall effect when encapsulated between *h*-BN layers.[58] In another report, a similar *h*-BN encapsulated few-layered b-P FET was found to display mobilities as high as ~45 000 cm^2 V^{-1} s^{-1} at 2 K in contrast to devices fabricated on Si/SiO_2 substrates which display low mobilities due to charged impurity scattering[5] in the SiO_2 layer. Hence, another objective of ours is to evaluate the electrical transport properties of the newly synthesized b-AsP FETs as a function of the temperature, which has yet to be explored. ESI Fig. S7a and S7b† shows I_{ds} measured at 4 K in a linear scale as a function of V_{bg} using both 2- and 4-terminal configurations. The threshold gate voltage for conduction shifts towards higher values when compared to the one measured near room temperature (Fig. 2e and f). This change in threshold gate voltage was also previously observed on WSe_2,[51,59] $MoTe_2$,[60] $MoSe_2$[61] and ReS_2[62] FETs fabricated on SiO_2 substrates. We attribute this shift in threshold gate voltages due to a combination of factors, such as disorder-induced localization at the interface with the SiO_2 layer, and a more prominent role for the Schottky barriers at the interface between metallic contacts and the semiconducting channel due to the suppression of thermionic processes. At any given gate voltage, the drain-to source current measured in a 4-terminal configuration, is always considerably higher than the one measured through a 2-terminal one, even at low

temperatures. This clearly indicates that contact resistance plays a significant role in the performance of the device throughout the entire temperature range from 300 K to 2 K.

Fig. S7c and S7d† display the same data as in Fig. S7a and S7b,† respectively but in a semi-logarithmic scale. Both, 2- and 4-terminal configurations indicate transistor current ON to OFF ratios of $\sim 10^4$–10^5 at $T = 4$ K, which is higher, by more than one order of magnitude, than the ratio measured at room temperature for the same device. The OFF current decreases considerably upon cooling down from room temperature, which is consistent with previous results in similar 2D devices.[63–65] A similar enhancement in ON/OFF current ratio by an order of 2, was reported for pristine black phosphorus at low temperatures.[66]

Fig. 3 shows the transport properties, including field-effect mobilities, as a function of the temperature for a few-layered b-AsP FET measured through 2- and 4-terminal configurations. Fig. 3a displays the two-terminal drain-to-source current I_{ds} as a function of V_{bg} under a constant bias V_{ds} = 15 mV for temperatures ranging from 250 K to 2 K. These measurements indicate that the threshold gate voltage for our b-AsP FET fabricated on a Si/SiO_2 substrate decreases from 40 V to 10 V when the temperature is reduced from 250 K to 10 K. This shift of the threshold gate-voltage by 30 V upon cooling from near room temperature to T = 10 K is likely due to the trapped carriers at the interface and the suppression of thermally activated detrapping.

The measured total current (I_{ds}) near room temperature is the sum of the currents resulting from the thermionic emission ($I_{thermal}$) and tunneling (I_{tunnel})[67] processes. As we cool down the device, the thermionic energy provided to the carriers decreases and the current becomes limited by the tunneling through the Schottky barriers formed between the metallic contacts and semiconducting b-AsP. Therefore, charge carriers become trapped at the interface unless the appropriate gate voltage is applied to overcome the barrier height.[51,59,61,62] The effect of impurities on the threshold gate-voltages was previously observed in devices fabricated from black phosphorus or other 2D semiconductors on Si/SiO_2 substrates.[5,51,60,62] Fig. 3b displays the I_{ds} as a function of V_{bg} measured through the 4-terminal configuration under a constant bias voltage V_{12} = 15 mV. The temperature dependent drain to source current, which is displayed in Fig. 3b, is again considerably higher than the one measured through the 2-terminal method. We observe an increase in the slope of I_{ds} as a function of V_{bg} with decreasing temperature. Despite the high contact resistance, the I_{ds} measured at low temperatures still show linear response as a function of V_{ds} with the I_{ds} as a function of V_{bg} showing an improved ON to OFF current ratio of up to $\sim 10^5$ as shown in the ESI (Fig. S8 and S9†).

From the previously discussed temperature dependence of I_{ds} as a function of V_{bg} data, we extracted the temperature dependence of the field-effect mobility for our few-layered b-AsP FETs using the MOSFET transconductance formula $\mu = \frac{L}{W}\frac{1}{C}\left(\frac{dI_{ds}}{dV_{bg}}\right)\frac{1}{V_{ds}}$, where L and W are the length and width of the channel respectively, C is the capacitance per unit area and V_{ds} is the drain-to-source voltage and where the slope is extracted *via* a linear fit. We obtained 2-terminal *hole*-mobilities for few-layered (~10 nm thick) b-AsP FETs as high as 200 $cm^2\ V^{-1}\ s^{-1}$. This value is very similar to mobility values reported for pristine bP[5,68] fabricated on SiO_2. This value is twice the mobility recently reported for b-AsP FET (83% As-doped crystal), namely 110 $cm^2\ V^{-1}\ s^{-1}$ for a 15 nm thick device.[25] Transport results from a second and a third FET fabricated from crystals having similar thicknesses are shown in the ESI (Fig. S10 and S11†) and found to yield a slightly lower mobility. Here, we focus on ~10 nm thick crystals without analyzing the thickness dependence of the transport properties. The threshold gate voltage is found to be sample dependent as seen by comparing Fig. S10† ($V_{th} \approx 60$ V) with Fig. S11† ($V_{th} \approx 40$ V). The temperature dependence of the 2-terminal mobility is shown in Fig. 3c (orange dots) and confirms that the conduction of carriers is indeed dominated by the resistance of the contacts and by the impurities at the interface. Initially, the mobility increases slightly as the temperature decreases from 250 K to 125 K due to the suppression of phonon scattering and then monotonically decreases as T is lowered down to 10 K before it saturates at a value of 120 $cm^2\ V^{-1}\ s^{-1}$ at T = 2 K. This decrease in mobility as a function of temperature is very similar to what has been observed in a number of TMDCs when fabricated on SiO_2 substrates[62,69–72] and results from the suppression of thermionic processes. The high temperature mobility as a function of T was fitted to the power law $\mu_{FE} \propto T^{-\gamma}$, where γ is the exponent characterizing the strength of the phonon scattering mechanism. The value of γ obtained from 2-terminal transport measurements is 0.18. Theoretically Ma and Jena *et al.*,[70,73] predicated that the charge carrier mobilities in 2D materials are highly dependent upon the dielectric environment and the density of impurities. Near room temperature, the mobility is dominated by phonon scattering, particularly optical phonons, when fabricated on SiO_2 substrates or a high κ – dielectric substrate such as *h*-BN, HfO_2 or Al_2O_3.[70] In our samples, As doping likely creates an additional, intrinsic disorder which ought to reduce the mobility at lower temperatures. Impurities and disorder created by As would be the major scattering factor decreasing its mobility. Nevertheless, as previously mentioned, these mobilities are close to those of pristine b-P, thus suggesting a very mild role for the disorder introduced by As-doping. Therefore, mobilities might increase if this material was surrounded by or encapsulated with a high κ – dielectric but this has yet to be done.

To minimize the role of the contacts in 2-terminal measurements, we evaluated the charge carrier mobility for our b-AsP FETs, also through 4-terminal measurements using the MOSFET formula $\mu = \left[\frac{l}{WC}\right]\left[d\left(\frac{I_{ds} - I_0}{V_{12}}\right)/dV_{bg}\right]$, where l is the channel length between the two voltage leads V_1 and V_2 as shown in the optical image, and W is the width of the channel. V_{12} is the voltage applied between both voltage leads. C is the capacitance per unit area and I_o is the off current of the transistor.[74,75] The temperature dependent carrier mobility obtained through 4-terminal measurements is shown in

 This journal is © The Royal Society of Chemistry 2019

Fig. 3c (red dots). As expected, the 4-terminal mobility is considerably higher than the one measured through the 2-terminal method, confirming that the resistance of the contacts is the dominant factor for carrier transport in 2D b-AsP. Our 4-terminal mobility measured at room temperature is ~300 $cm^2 V^{-1} s^{-1}$, which is three times higher than the mobility reported for a FET based on a 15 nm thick crystal of 83% As doped b-AsP.[25] The lower mobility reported in ref. 21 could result from contact resistance in their 2-terminal measurements and/or it could result from the higher As concentration.

The 4-terminal mobility increases sharply as a function of decreasing temperature down to 100 K. Below 100 K the mobility nearly saturates to values between 550–600 $cm^2 V^{-1} s^{-1}$. We fitted the mobility at higher temperatures, *i.e.* from T = 100 K to 300 K, to a power law, $\mu = T^{-\gamma}$, obtaining γ = 1.5. This value is much higher than the 2-terminal one, discussed above, but similar to values reported for other 2D materials such as MoS_2, WSe_2, and ReS_2.[50,51,62] Although our devices were fabricated on Si/SiO_2 substrates, this value is relatively close to γ = 2 obtained for pristine bP on *h*-BN substrates,[21] and much higher than γ = 0.5 for pristine b-P also on SiO_2 substrates.[5] This difference may be due to differences in device quality or interface scattering which affects the mobility. Thinner samples are more susceptible to charged impurities at the interface that otherwise can be screened by induced charges in thicker samples. This large γ value strongly suggests dominant optical phonon scattering in this temperature regime in our few-layered As-bP device. The saturation of the mobility below 100 K results from scattering by impurities and trap states at the interface with the SiO_2 substrate in the absence of thermionic emission processes.[69,70] The much higher exponent obtained with the 4-terminal configuration is due to the much higher currents extracted when using it. In this configuration, the extracted currents result from the bias voltage exciting only the semiconducting channel. While for the 2-terminal configuration the bias voltage is applied to both current leads, whose resistance is temperature dependent, as well as the semiconducting channel, hence necessarily leading to much smaller currents. Through the minimization of the role of the contacts one ends up extracting a more accurate value for γ.

We analyzed the transport properties as a function of the temperature within the framework of the 2D variable range hopping mechanism as presented in Fig. 3d. As seen, the data agrees well with the 2D VRH expression $\sigma(T) = \sigma_o(T)\exp(-T_o/T)^{1/(1+d)}$ where σ is the conductivity, d is the dimensionality of the system and $T_o = \frac{18.1\alpha^3}{k_B D(E_F)}$ is a characteristic energy scale that depends on the density of states $D(E_F)$. Here, we assumed d = 2 although the thickness of the measured device is ~10 nm. This assumption is further supported by the recent observation of quantum oscillations due to the two dimensional hole gas confined at the interface between the b-AsP and the SiO_2 layer due to the applied gate electric field.[76–79] The agreement with the 2D VRH mechanism indicates that hole transport in few layered b-AsP occurs in a wide energy band of localized states, rather than through the direct promotion of carriers to the valence band maximum or towards the mobility edge with respect to the Fermi energy.[76] The slope of the linear fits, *i.e.* red lines in Fig. 3d, decreases with increasing negative gate voltage, which indicates that the value of T_o decreases, or that the density of carriers increases. For MoS_2 it was suggested that charges trapped at the surface of the SiO_2 layer beneath the thin MoS_2 crystals generate random localized potential wells.[76] This analogy can also be applied to our b-AsP samples where the 2D hole-gas would form at the interface with the SiO_2 layer upon gating. Notice that site disorder due to substitutional As, should also contribute to the disorder in this system. The electrical current flowing through the interface between the metallic contact and the semiconducting channel is usually non-linear with respect to the applied bias voltage due to their band misalignment which leads to a Schottky barrier (SB). The flow of current mostly depends on the magnitude of the SB, which, in addition to band misalignment, is affected by the formation of dipolar states, the quality of the metallization, and chemical residues at their interface. To extract the height of the Schottky barrier at the Ti : Au and b-AsP interface, we carefully re-analyzed the temperature dependence of the conductivity previously shown in Fig. 3a and b and as discussed in Fig. 4.

Fig. 4a shows the I_{ds} as a function of V_{bg}–V_T at several temperatures ranging from 250 to 2K measured through a 4-terminal configuration, where V_T is the threshold gate voltage measured with the smallest current. It is clear that there is an increase in conductivity with decreasing temperature from 250 to 25 K while the conductivity seems to slightly decrease below 25 K. This suggests that the mobility of the sample increases as a function of decreasing temperature, due to a gate induced insulator to metal phase-transition as previously reported in other 2D TMDCs.[62,80] We extracted the resistivity as a function of the temperature from Fig. 4a at V_{bg}–V_T = −60 V as presented in the ESI Fig. S12.† From room temperature down to 100 K the resistivity shows a positive slope $\frac{d\rho}{dT} > 0$, indicating metallic behavior. Below 100 K the resistivity remains nearly constant. This overall behavior is consistent with a gate-induced 2D metal to insulator phase transition.[81] The saturation of resistivity observed below 100 K would be attributable to disorder. Fig. 4(b–d) illustrates the extraction of the Schottky barrier height as a function of the gate voltage for our b-AsP FET measured through both 2- and 4-terminal configurations. We analyzed the data using thermionic emission theory according to the following equation:

$$I_{ds} = AA^*T^{3/2} \exp\left[(q\phi_{eff}/k_B T)\right]$$

where A^* is the Richardson constant, q is the charge of the electron, k_B is the Boltzmann constant and ϕ_{eff} is the effective Schottky barrier height. Fig. 4b and c show Arrhenius plots of $\ln(I_{ds}/T^{3/2})$ as a function of $q/k_B T$ for 2- and 4-terminal measurements, respectively. Here, we fit only the high temperature data to a linear-fit, given that this temperature region is dominated by the thermionic emission contribution. We observed that the slope of the $\ln(I_{ds}/T^{3/2})$ as a function of $q/k_B T$

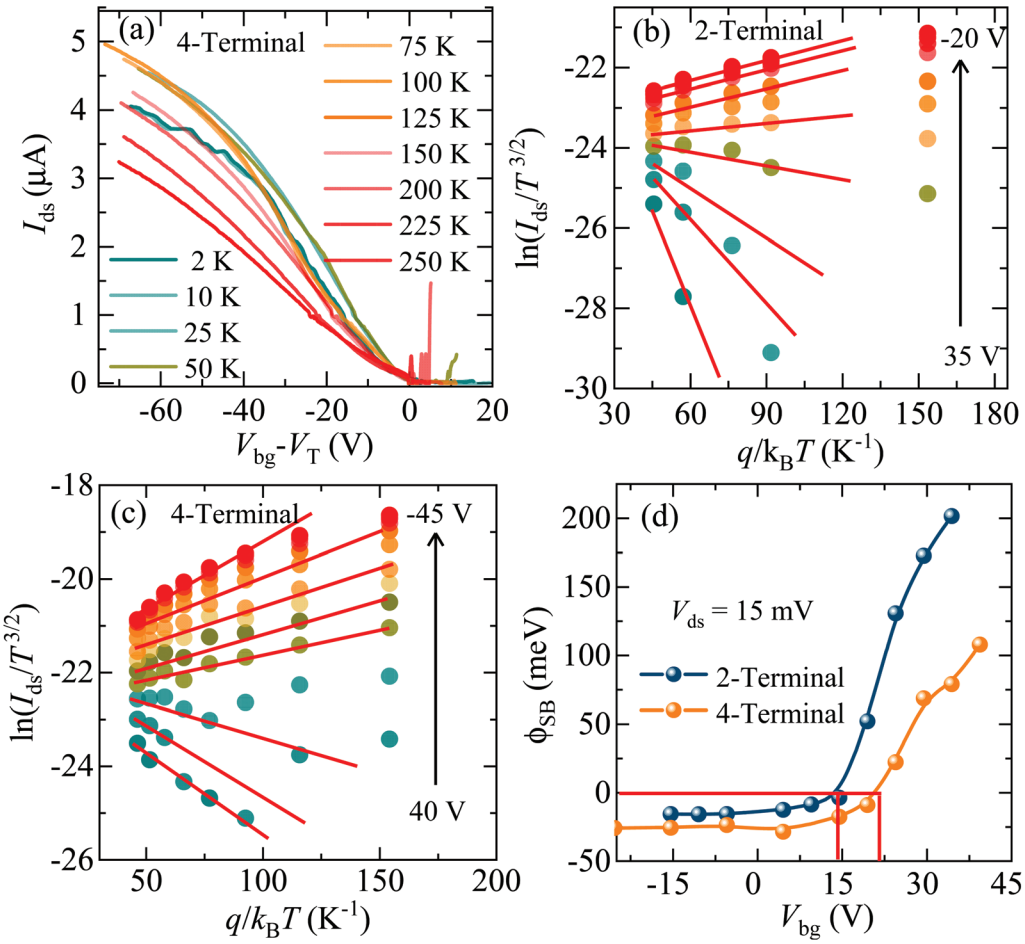

Fig. 4 (a) Drain to source current I_{ds}, as a function of $V_{bg}-V_T$ for the device measured through the 4-terminal method, data from Fig. 5b. V_T is the voltage at the minimum current measured. (b) and (c) $I_{ds}T^{-3/2}$ as a function of q/k_BT including linear fits to the data collected under several gate voltages ranging from V_{bg} = 35 V to −20 V, and for 2- and 4-terminal configurations, respectively. (d) Schottky barrier height extracted from panels (b) and (c) as a function of the gate voltage. Notice that at high negative gate voltages we obtain non physical values for the Schottky barrier, since this system behaves as a metal.

for several values of V_{bg} changes from negative (at positive gate voltages) to positive (at negative gate voltages) as similarly reported for a Ni/Au contacted b-P FET[76] or b-P devices with graphene contacts.[82]

The extracted effective SBH is shown in Fig. 4d as a function of the gate voltage for both 2- and 4-terminal measurements. For V_{bg} < 17 V we observed small (<25 meV) and negative Schottky barrier height for both 2- and 4-terminal measurements, likely reflecting the metallic character of the sample. In the OFF state of the transistor, or for >V_{bg} = 15 V, the barrier height increases sharply from nearly 0 meV at V_{bg} = 15 V up to 200 meV under V_{bg} = 35 V for the 2-terminal configuration. And from 0 meV under V_{bg} = 22 V up to 100 meV at V_{bg} = 40 V for the 4-terminal one. For V_{bg} < 15 V (2-terminal) or V_{bg} < 22 V (4-terminal), negative Schottky barrier heights were extracted though the above classical thermionic emission model. Similar negative values were reported by Li *et al.*[80] when using Ni/Au contacts, indicating that thermionic emission fails in the metallic state due to the absence of a band gap. Negative Schottky barrier heights were also reported for pristine black phosphorus FETs using graphene and metallic contacts.[2,80–84] Avsar *et al.* reported negative SBH for a *h*-BN encapsulated b-P FET for all gate voltages using graphene as contact material.[82] Previous studies observing negative SB are based on samples using graphene and magnetic metals for the contacts, which are known to form better contacts with the 2D semiconducting channel than other traditional metallic contacts. In our case, and according to our calculations, doping with As leads to a displacement of the chemical potential towards the valence band maximum, which facilitates the stabilization of a metallic state upon gating, and hence to the suppression of the SB at the interface between b-AsP and Ti. Therefore, negative values would have no physical meaning and reflect the metallic character of our sample upon gating.

Before proceeding with discussing additional experimental results, we need to briefly discuss our band structure calculations and their implications. Much more detail can be found in the Methods section and in the ESI.† The equilibrium 2D

 This journal is © The Royal Society of Chemistry 2019

layered structure of the single layer (1L), bi-layers (2L), tri-layers (3L) of 25% As-doped black phosphorous (b-AsP), and of the bulk crystal structure b-AsP were calculated by employing *ab initio* first-principles based hybrid density functional theory calculations; the HSE06-D method which is shown in Fig. S6 in the ESI.† The electronic properties of these materials, *i.e.* band structures of 1L, 2L, 3L b-AsP, and of the bulk crystal structure of b-AsP were computed *via* the same method with the band structure for the monolayer shown in Fig. S6 and Table S3.† The present computation found that the electronic band gap (E_g) depends on the number of b-AsP layers (*i.e.* 1L, 2L, 3L and bulk) and that E_g increases gradually from the bulk crystal to the monolayer limit b-AsP. This calculation indicates that the band gap E_g is inversely proportional to the number of layers of b-AsP. A direct band gap of about 0.21 eV emerges at the Γ-point in the band structure of the bulk crystal of b-AsP. The band gap of the 3L b-AsP increases by 0.63 eV when compared to the bulk crystal. Similarly, for the 2L b-AsP E_g increases by 0.913 eV at the Γ-point. The highest direct band gap was observed for the monolayer b-AsP with a band gap at the Γ-point of about 1.305 eV. The computed electronic band gap of the monolayer, 2L, 3L and bulk are 1.58 eV, 1.123 eV, 0.84 eV and 0.21 eV respectively. These values are tabulated in Table S3 within the ESI.† Most importantly, the position of the top of the valence band at the Γ-point with respect to the Fermi level is calculated as: −1 meV for pristine bulk b-P, −3 meV for bulk b-AsP, and 5.8, 3 and 4 meV for 3L, 2L, and 1L b-AsP, respectively. Therefore, the calculations indicate that

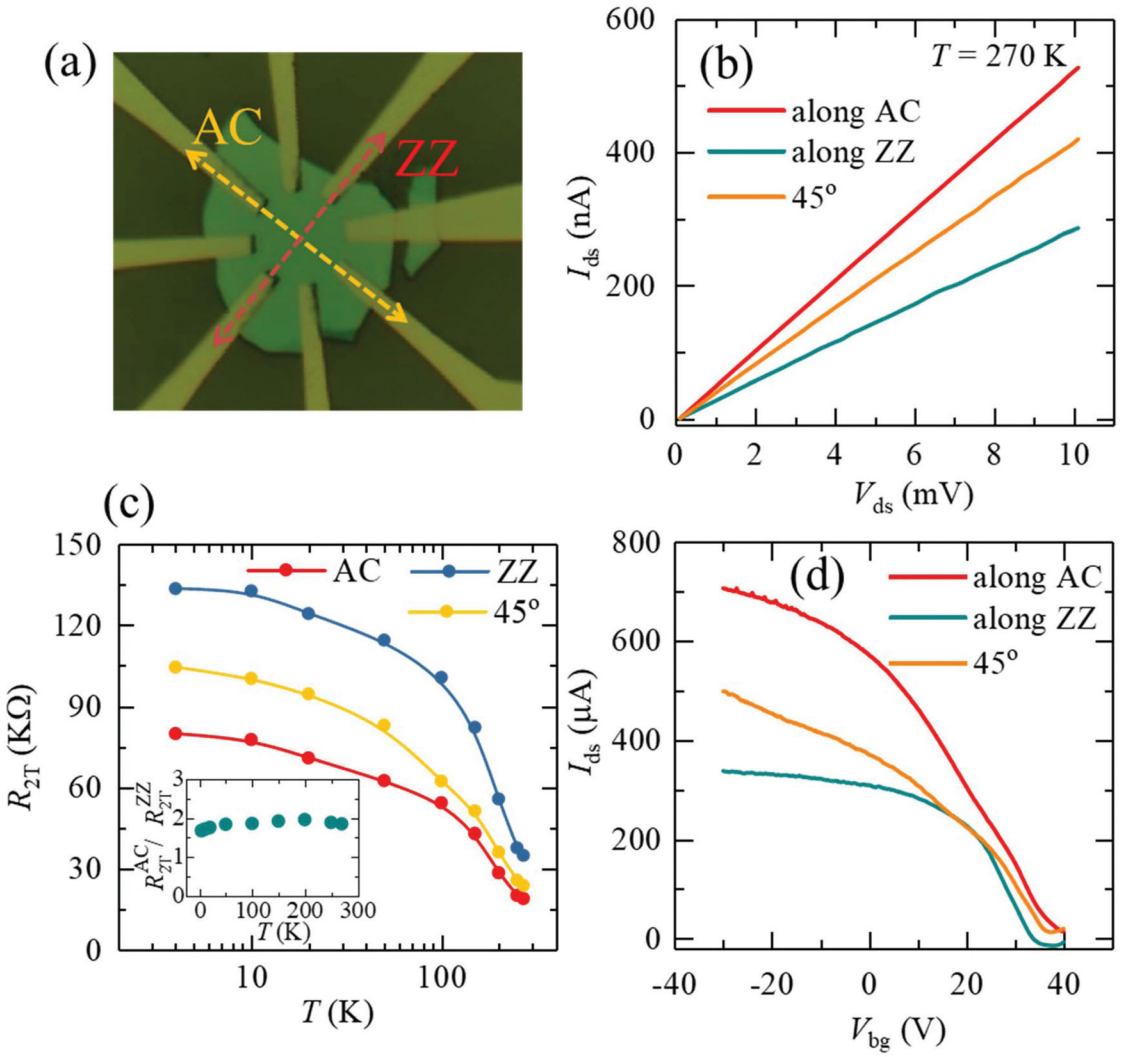

Fig. 5 (a) Optical image of a multi-terminal As-bP FET designed for measuring the transport anisotropy. It is composed of 4-pairs of equally spaced Ti : Au contacts with a distance l = 8.1 μm between opposite pairs (channel length). Arm-chair (AC) and zig-zag crystal axes are indicated and identified from the transport measurements through a comparison with pristine b-P devices. (b) I_{ds} collected along three different directions of the crystal, namely along the AC, ZZ axes and along a 45° direction with respect to both axes as a function of V_{ds}. These traces were measured at T = 270 K under an applied gate voltage V_{bg} = −40 V. (c) Anisotropy of the resistance ($R = V_{ds}/I_{ds}$), as extracted from I_{ds} as a function of V_{ds} characteristics, and as a function of the temperature. Inset: ratio of the resistance R_{2T}^{AC}/R_{2T}^{ZZ} as a function of temperature. (d) I_{ds} as a function of V_{bg} at T = 150 K and under V_{ds} = 30 mV.

the Fermi lies very close to the edge of the valence band. Hence, one should expect these compounds to display a tendency to behave as hole-doped upon gating, as observed here. Nevertheless, their response can also depend on the deformation of the bands around the electrical contact area due to the formation of the Schottky barriers.

Finally, we studied the anisotropy in the transport properties of few-layered b-AsP. For this experiment 4 evenly spaced pairs of Ti : Au (5 nm:70 nm) electrodes were fabricated on a few layered (~12 nm thick) b-AsP crystal, with each pair forming an angle of 45° with respect to the neighboring ones, as shown in Fig. 5a. We measured the transport curves for each pair of opposite electrodes having a width ≅1.3 μm which are separated by l ~8.1 μm. The dashed lines are nearly aligned along the armchair (AC) and the zig-zag (ZZ) axes of the crystal. The I_{ds} as a function of V_{ds} traces measured at T = 270 K under V_{bg} = −40 V are displayed in the Fig. 5b and yield the anisotropy of the conductivity. The current measured along the AC direction is 2.3 times higher than the one measured along the ZZ direction under an excitation V_{ds} = 10 mV. Fig. 5c shows the temperature dependence of the resistance, $R_{2T} = V_{ds}/I_{ds}$ from the I_{ds} as a function of V_{ds} characteristics for currents flowing along both the AC and the ZZ directions and at an angle of 45° between both axes. The inset of Fig. 5c shows the ratio of the resistance measured for currents flowing along both the armchair and the zig-zag axes (R_{2T}^{AC}/R_{2T}^{ZZ}). It turns out that b-AsP shows a nearly constant anisotropy of 2 over the entire temperature range.

We extracted the anisotropy of the conductivity at several temperatures from the I_{ds} as a function of V_{ds} data, obtaining an anisotropy of ~2 between currents flowing along the AC-with respect to the ZZ-direction. Fig. 5d depicts the I_{ds} measured at 150 K as a function of V_{bg} under a bias voltage V_{ds} = 30 mV. The ratio of the drain to source current between both axis, *i.e.* I_{ds}^{AC}/I_{ds}^{ZZ}, varies slightly as a function of the gate voltage. We measured the ratio I_{ds}^{AC}/I_{ds}^{ZZ} from V_{bg} = 20 to −30 V finding values around 1.8–2.2. In the OFF state of the transistor, or for ~V_{bg} = 35 V, it reaches a ratio of ~7. In Fig. S13† we provide a micrograph of a second device having the same configuration of contacts and whose I–V characteristics (also included in Fig. S13†) yields anisotropy of 1.8 This anisotropy measured in two devices is similar to the anisotropic of the conductivity measured for ReS_2, whose anisotropy was used to create an inverter application.[33] The electrical anisotropy for a 2nd device at room temperature is shown in the electronic supporting section (Fig. S14†), I_{ds} *vs.* V_{ds}. The anisotropy in the mobility measured for a pristine b-P crystal by Xia *et al.*[18] is 1.5. Similar to the anisotropy of the electrical conductivity, the anisotropy of the planar thermal conductivity was also measured and found to be 1.5.[53] The slightly higher anisotropy obtained here could result from the particular As clustering proposed for this compound (see, Fig. 1(b)). The anisotropy of the thermal conductivity in b-AsP crystals has yet to be investigated for potential applications in thermoelectric devices. The anisotropy in conductivity might yield unique technological applications in electronics or optoelectronics. For example, ReS_2 displays anisotropic transport yielding an anisotropy of 7, for currents flowing along the *b*-axis when compared to currents applied along the *a*-axis, which led to the design of a unique inverter for logic applications.[53]

Conclusion

In conclusion, we studied the Raman and the polarization dependence of the Raman scattering in few layered As-doped black-phosphorus with an As concentration of 25%. Using *ab initio* hybrid density functional theory calculations (HSE06-D method), we investigated the electronic properties of the monolayer, 2L, 3L and bulk crystal structure of b-AsP. To first approximation, the Raman measured modes are similar to those previously extracted for pristine b-P but multiplied by a factor of 3 due to the existence of P–P, As–P, As–As bonds. Based on density functional perturbation theory (DFPT), we also provide a theoretical calculation capturing and indexing the observed Raman modes. Nevertheless, these Raman calculations could not capture the correct evolution of the modes as a function of the As concentration. We explored the temperature dependence of the electrical transport properties of b-AsP FETs fabricated on Si/SiO_2 substrates. For crystals composed of nearly 10 atomic layers, we find that the intrinsic mobility measured at room temperature approaches 300 $cm^2\ V^{-1}\ s^{-1}$ increasing to 600 $cm^2\ V^{-1}\ s^{-1}$ at 100 K and remaining nearly constant as the temperature is reduced to 2 K. Remarkably, these values are similar to those reported for pristine b-P crystals of similar thicknesses, indicating that As doping up to 25% does not seriously compromise the transport properties of b-P. The transport properties are found to be anisotropic with the anisotropy being gate-voltage dependent and ranging from 2 to 7. These anisotropy values are slightly higher or similar to those reported for pristine b-P or for ReS_2. Encapsulating the device with a suitable high κ-dielectric material should increase the mobility of the b-AsP, which could open the door for studying the physics of a disordered anisotropic 2D electron gas at low temperatures in order to contrast with the response of pristine black phosphorus. The ability to tune its band gaps as function of the number of layers (gap increases as the number of layers decrease) and as a function of As doping (gap decreases as a function of As doping) provides two handles to adjust its optoelectronic properties for niche applications, for example, as photo-sensors detecting light from the visible to the infrared region of the electromagnetic spectrum. A final word concerning the ability to tune this system towards a metallic state with a gate voltage: the close proximity of the Fermi level to the edge of the valence band indicates that it should be quite possible to locally (*e.g.* around the electrical contact area(s)) tune the system to a metallic state with independent local gates and in this way nearly suppress the Schottky barriers at the current contacts. This should increase the performance of few-layered b-AsP FETs, which as we have shown here display nearly the same mobilities as pristine black phosphorus. Hence, Arsenic

 This journal is © The Royal Society of Chemistry 2019

doped bP crystals may lead to unique logic applications that explore its anisotropic nature once degradation is prevented through the use of capping layers.

Author contributions

NRP and LB conceived the project. NDZ synthesized the b-AsP single crystals. NRP, JM, DR, RD, AS fabricated the field-effect transistor devices. NRP and JM measured temperature dependent transport properties and NRP analyzed the electrical transport data, CG, NRP, SM performed Raman and Polarization dependent Raman measurements. MCL and HT contributed theoretical Raman calculation as a function of As contents. SP and JLM contributed theoretical band structure calculation as a function of number of layers. NRP and LB wrote the manuscript with the input of all co-authors.

Conflicts of interest

The authors declare no competing financial interests.

Acknowledgements

N. R. P. acknowledged NSF-PREM through NSF-DMR # 1826886, HBCU-UP Excellence in research NSF-DMR # 1900692. This work was performed, in part, at the Center for Nanoscale Materials, a U.S. Department of Energy Office of Science User Facility, and supported by the U.S. Department of Energy, Office of Science, under Contract No. DE-AC02-06CH11357. L. B. acknowledges support from NSF-DMR # 1807969. M. C. L. and H. T. are grateful to the National Science Foundation (EFRI-1433311). The supercomputer time was provided by the Center for Computational Innovations (CCI) at Rensselaer Polytechnic Institute and the Extreme Science and Engineering Discovery Environment (XSEDE, project TG-DMR17008), which is supported by National Science Foundation grant number ACI-1053575. J. L. M.-C. was supported by Florida State University (FSU). The authors gratefully acknowledge the support from the Energy and Materials Initiative and the High Performance Material Institute (HPMI) facilities at FSU. S. P. thanks the SERB-DST, Govt. of India for providing the Ramanujan Faculty Fellowship under the Grant No. SB/S2/RJN-067/2017. A portion of this work was performed at the National High Magnetic Field Laboratory, which is supported by National Science Foundation Cooperative Agreement No. DMR-1644779 and the State of Florida. The authors thank the High Performance Computer cluster at the Research Computing Center (RCC), FSU, for providing computational resources and support.

References

1 I. Ferain, C. A. Colinge and J.-P. Colinge, *Nature*, 2011, **479**, 310–316.
2 X. Cui, G. H. Lee, Y. D. Kim, G. Arefe, P. Y. Huang, C. H. Lee, D. A. Chenet, X. Zhang, L. Wang, F. Ye and F. Pizzocchero, *Nat. Nanotechnol.*, 2015, **10**, 534–540.
3 M. Batmunkh, M. Bat-Erdene and J. G. Shapter, *Adv. Mater.*, 2016, **28**, 8586–8617.
4 E. Flores, J. R. Ares, A. Castellanos-Gomez, M. Barawi, I. J. Ferrer and C. Sánchez, *Appl. Phys. Lett.*, 2015, **106**, 022102.
5 L. Li, Y. Yu, G. J. Ye, Q. Ge, X. Ou, H. Wu, D. Feng, X. H. Chen and Y. Zhang, *Nat. Nanotechnol.*, 2014, **9**, 372–377.
6 J. Dai and X. C. Zeng, *J. Phys. Chem. Lett.*, 2014, **5**, 1289–1293.
7 Z. Zhang, X. Xin, Q. Yan, Q. Li, Y. Yang and T. L. Ren, *Sci. China Mater.*, 2016, **59**, 122–134.
8 Y. Huang, J. Qiao, K. He, S. Bliznakov, F. Sutter, X. Chen, D. Luo, F. Meng, D. Su, J. Decker, W. Ji, R. S. Ruoff and P. Sutter, *Chem. Mater.*, 2016, **28**, 8330–8339.
9 H. Guo, N. Lu, J. Dai, X. Wu and X. C. Zeng, *J. Phys. Chem. C*, 2014, **118**, 14051–14059.
10 Y. Cai, Z. Zhang and Y.-W. Zhang, *Sci. Rep.*, 2014, **4**, 6677.
11 M. Buscema, D. J. Groenendijk, G. A. Steele, H. S. J. van der Zant and A. Castellanos-Gomez, *Nat. Commun.*, 2014, **5**, 4651.
12 H. Liu, Y. Du, Y. Deng and P. D. Ye, *Chem. Soc. Rev.*, 2015, **44**, 2732–2743.
13 M. Engel, M. Steiner and P. Avouris, *Nano. Lett.*, 2014, **14**, 6414–6417.
14 W. Zhu, M. N. Yogeesh, S. Yang, S. H. Aldave, J.-S. Kim, S. Sonde, L. Tao, N. Lu and D. Akinwande, *Nano Lett.*, 2015, **15**, 1883–1890.
15 W. Xia, Q. Zhang, F. Xu, H. Ma, J. Chen, K. Qasim, B. Ge, C. Zhu and L. Sun, *J. Phys. Chem. C*, 2016, **120**, 5861–5868.
16 C. Hao, B. Yang, F. Wen, J. Xiang, L. Li, W. Wang, Z. Zeng, B. Xu, Z. Zhao, Z. Liu and Y. Tian, *Adv. Mater.*, 2016, **28**, 3194–3201.
17 H. Wang, X. Yang, W. Shao, S. Chen, J. Xie, X. Zhang, J. Wang and Y. Xie, *J. Am. Chem. Soc.*, 2015, **137**, 11376–11382.
18 F. Xia, H. Wang and Y. Jia, *Nat. Commun.*, 2014, **5**, 4458.
19 H. Liu, A. T. Neal, Z. Zhu, Z. Luo, X. Xu, D. Tománek and P. D. Ye, *ACS Nano*, 2014, **8**, 4033–4041.
20 X. Ling, H. Wang, S. Huang, F. Xia and M. S. Dresselhaus, *Proc. Natl. Acad. Sci. U. S. A.*, 2015, **112**, 4523–4530.
21 G. Long, D. Maryenko, J. Shen, S. Xu, J. Hou, Z. Wu, W. K. Wong, T. Han, J. Lin, Y. Cai and R. Lortz, *Nano Lett.*, 2016, **16**, 7768–7773.
22 J. Kim, S. S. Baik, S. H. Ryu, Y. Sohn, S. Park, B.-G. Park, J. Denlinger, Y. Yi, H. J. Choi and K. S. Kim, *Science*, 2015, **349**, 723–726.
23 U. Häussermann, *Chem. – Eur. J.*, 2003, **9**, 1471–1478.
24 O. Osters, T. Nilges, F. Bachhuber, F. Pielnhofer, R. Weihrich, M. Schöneich and P. Schmidt, *Angew. Chem., Int. Ed.*, 2012, **51**, 2994–2997.
25 B. Liu, M. Köpf, A. N. Abbas, X. Wang, Q. Guo, Y. Jia, F. Xia, R. Weihrich, F. Bachhuber, F. Pielnhofer, H. Wang, R. Dhall, S. B. Cronin, M. Ge, X. Fang, T. Nilges and C. Zhou, *Adv. Mater.*, 2015, **27**, 4423–4429.

This journal is © The Royal Society of Chemistry 2019

26 Y. Xu, J. Yuan, L. Fei, X. Wang, Q. Bao, Y. Wang, K. Zhang and Y. Zhang, *Small*, 2016, **12**, 5000–5007.
27 Y. Ge, S. Chen, Y. Xu, Z. He, Z. Liang, Y. Chen, Y. Song, D. Fan, K. Zhang and H. Zhang, *J. Mater. Chem. C*, 2017, **5**, 6129–6135.
28 B. Yang, B. Wan, Q. Zhou, Y. Wang, W. Hu, W. Lv, Q. Chen, Z. Zeng, F. Wen, J. Xiang, S. Yuan, J. Wang, B. Zhang, W. Wang, J. Zhang, B. Xu, Z. Zhao, Y. Tian and Z. Liu, *Adv. Mater.*, 2016, **28**, 9408–9415.
29 Z. Zhang, M. Khurram, Z. Sun and Q. Yan, *Inorg. Chem.*, 2018, **57**, 4098–4103.
30 C. C. Mayorga-Martinez, Z. Sofer, D. Sedmidubský, J. Luxa, B. Kherzi and M. Pumera, *Nanoscale*, 2018, **10**, 1540.
31 P. K. Sarswat, S. Sarkar, J. Cho, D. Bhattacharyya and M. L. Free, *ECS J. Solid State Sci. Technol.*, 2016, **5**, Q3026–Q3032.
32 P. K. Sarswat, S. Sarkar, D. Bhattacharyya, J. Cho and M. L. Free, *Ceram. Int.*, 2016, **42**, 13113–13127.
33 E. Liu, Y. Fu, Y. Wang, Y. Feng, H. Liu, X. Wan, W. Zhou, B. Wang, L. Shao, C. Ho and Y. S. Huang, *Nat. Commun.*, 2015, **6**, 6991.
34 I. Shirotani, J. Mikami, T. Adachi, Y. Katayama, K. Tsuji, H. Kawamura, O. Shinomura and T. Nakajima, *Phys. Rev. B: Condens. Matter Mater. Phys.*, 1994, **50**, 16274–16278.
35 F. Shojaei and H. S. Kang, *J. Phys. Chem. C*, 2015, **119**, 20210–20216.
36 P. Giannozzi, S. Baroni, N. Bonini, M. Calandra, R. Car, C. Cavazzoni, D. Ceresoli, G. L. Chiarotti, M. Cococcioni, I. Dabo, A. Dal Corso, S. Fabris, G. Fratesi, S. de Gironcoli, R. Gebauer, U. Gerstmann, C. Gougoussis, A. Kokalj, M. Lazzeri, L. Martin-Samos, N. Marzari, F. Mauri, R. Mazzarello, S. Paolini, A. Pasquarello, L. Paulatto, C. Sbraccia, S. Scandolo, G. Sclauzero, A. P. Seitsonen, A. Smogunov, P. Umari and R. M. Wentzcovitch, *J. Phys.: Condens. Matter*, 2009, **21**, 395502.
37 M. Lazzeri and F. Mauri, *Phys. Rev. Lett.*, 2003, **90**, 36401.
38 J. Heyd, J. E. Peralta, G. E. Scuseria, R. L. Martin and R. L. The, *J. Chem. Phys.*, 2005, **123**, 174101.
39 R. Dovesi, R. Orlando, A. Erba, C. M. Zicovich-Wilson, B. Civalleri, S. Casassa, L. Maschio, M. Ferrabone, M. De La Pierre and E. A. D'Arco, *Int. J. Quantum Chem.*, 2014, **114**, 1287–1317.
40 S. Grimme, J. Antony, S. Ehrlich and H. Krieg, *J. Chem. Phys.*, 2010, **132**, 154104.
41 S. Pakhira, K. P. Lucht and J. L. Mendoza-Cortes, *J. Chem. Phys.*, 2018, **148**, 064707.
42 S. Pakhira and J. L. Mendoza-Cortes, *J. Phys. Chem. C*, 2018, **122**, 4768–4782.
43 S. Pakhira, K. P. Lucht and J. L. Mendoza-Cortes, *J. Phys. Chem. C*, 2017, **121**, 21160.
44 W. Niu, S. Pakhira, K. Marcus, Z. Li, J. L. Mendoza-Cortes and Y. Yang, *Adv. Energy Mater.*, 2018, **8**, 1800480.
45 M. F. Peintinger, D. V. Oliveira and T. Bredow, *J. Comput. Chem.*, 2013, **34**, 451–459.
46 J. Baker, A. Scheiner and J. Andzelm, *Chem. Phys. Lett.*, 1993, **216**, 380–388.
47 A. Montoya, T. N. Truong and A. F. Sarofim, *J. Phys. Chem. A*, 2000, **104**, 6108–6110.
48 S. Pakhira, R. I. Singh, O. Olatunji-Ojo, M. Frenklach and W. A. Lester Jr., *J. Phys. Chem. A*, 2016, **120**, 3602–3612.
49 H. J. Monkhorst and J. D. Pack, *Phys. Rev. B: Solid State*, 1976, **13**, 5188–5192.
50 K. Momma and F. Izumi, *J. Appl. Crystallogr.*, 2011, **44**, 1272–1276.
51 N. R. Pradhan, D. Rhodes, S. Memaran, J. M. Poumirol, D. Smirnov, S. Talapatra, S. Feng, N. Perea-Lopez, A. L. Elias, M. Terrones, P. M. Ajayan and L. Balicas, *Sci. Rep.*, 2015, **5**, 8979.
52 Y. Du, H. Liu, Y. Deng and P. D. Ye, *ACS Nano*, 2014, **8**, 10035–10042.
53 Z. Luo, J. Maassen, Y. Deng, Y. Du, R. P. Garrelts, M. S. Lundstrom, P. D. Ye and X. Xu, *Nat. Commun.*, 2015, **6**, 8572.
54 X. Wang, A. M. Jones, K. L. Seyler, V. Tran, Y. Jia, H. Zhao, H. Wang, L. Yang, X. Xu and F. Xia, *Nat. Nanotechnol.*, 2015, **10**, 517–521.
55 W. J. Yin, T. Shi and Y. Yan, *Appl. Phys. Lett.*, 2014, **104**, 063903.
56 CYTOP® | Product information | Fluoroproducts Business | AGC Chemicals Company. Available at: https://www.agc-chemicals.com/jp/en/fluorine/products/detail/index.html?pCode=JP-EN-F019.
57 Y. Deng, N. J. Conrad, Z. Luo, H. Liu, X. Xu and D. Y. Peide, *IEEE Int.*, 2014, 5.2.1–5.2.4.
58 L. Li, F. Yang, G. J. Ye, Z. Zhang, Z. Zhu, W. Lou, X. Zhou, L. Li, K. Watanabe, T. Taniguchi and K. Chang, *Nat. Nanotechnol.*, 2016, **11**, 593.
59 N. R. Pradhan, J. Ludwig, Z. Lu, D. Rhodes, M. M. Bishop, K. Thirunavukkuarasu, S. A. McGill, D. Smirnov and L. Balicas, *ACS Appl. Mater. Interfaces*, 2015, **7**, 12080–12088.
60 N. R. Pradhan, D. Rhodes, S. Feng, Y. Xin, S. Memaran, B. H. Moon, H. Terrones, M. Terrones and L. Balicas, *ACS Nano*, 2014, **8**, 5911–5920.
61 N. R. Pradhan, Z. Lu, D. Rhodes, D. Smirnov, E. Manousakis and L. Balicas, *Adv. Electron. Mater.*, 2015, **1**, 1500215.
62 N. R. Pradhan, A. McCreary, D. Rhodes, Z. Lu, S. Feng, E. Manousakis, D. Smirnov, R. Namburu, M. Dubey, A. R. Hight Walker, H. Terrones and L. Balicas, *Nano Lett.*, 2015, **15**, 8377–8384.
63 J. Kang, D. Jariwala, C. R. Ryder, S. A. Wells, Y. Choi, E. Hwang, J. H. Cho, T. J. Marks and M. C. Hersam, *Nano Lett.*, 2016, **16**, 2580–2585.
64 M. V. Kamalakar, B. N. Madhushankar, A. Dankert and S. P. Dash, *Small*, 2015, **11**, 2209–2216.
65 F. Xia, D. B. Farmer, Y. M. Lin and P. Avouris, *Nano Lett.*, 2010, **10**, 715–718.
66 S. Liang, H. Yang, A. Djeffal, B. Tao, S. Mc-Murtry, S. Mangin and Y. Lu, *J. Appl. Phys.*, 2017, **122**, 164301.
67 A. Prakash, H. Ilatikhameneh, P. Wu and J. Appenzeller, *Sci. Rep.*, 2017, **7**, 12596.

 This journal is © The Royal Society of Chemistry 2019

68 H. S. Ra, A. Y. Lee, D. H. Kwak, M. H. Jeong and J. S. Lee, *ACS Appl. Mater. Interfaces*, 2017, **10**, 925–932.
69 M. Y. Chan, K. Komatsu, S. L. Li, Y. Xu, P. Darmawan, H. Kuramochi, S. Nakaharai, A. Aparecido-Ferreira, K. Watanabe, T. Taniguchi and K. Tsukagoshi, *Nanoscale*, 2013, **5**, 9572–9576.
70 N. Ma and D. Jena, *Phys. Rev. X*, 2014, **4**, 011043.
71 M. W. Lin, I. I. Kravchenko, J. Fowlkes, X. Li, A. A. Puretzky, C. M. Rouleau, D. B. Geohegan and K. Xiao, *Nanotechnology*, 2016, **27**, 165203.
72 S. Sucharitakul, N. J. Goble, U. R. Kumar, R. Sankar, Z. A. Bogorad, F. C. Chou, Y. T. Chen and X. P. Gao, *Nano Lett.*, 2015, **15**, 3815–3819.
73 K. Kaasbjerg, K. S. Thygesen and K. W. Jacobsen, *Phys. Rev. B: Condens. Matter Mater. Phys.*, 2012, **85**, 115317.
74 W. Bao, X. Cai, D. Kim, K. Sridhara and M. S. Fuhrer, *Appl. Phys. Lett.*, 2013, **102**, 042104.
75 S. Larentis, B. Fallahazad and E. Tutuc, *Appl. Phys. Lett.*, 2012, **101**, 223104.
76 S. Ghatak, A. N. Pal and A. Ghosh, *ACS Nano*, 2011, **5**, 7707–7712.
77 X. Chen, Y. Wu, Z. Wu, Y. Han, S. Xu, L. Wang, W. Ye, T. Han, Y. He, Y. Cai and N. Wang, *Nat. Commun.*, 2015, **6**, 7315.
78 V. Tayari, N. Hemsworth, I. Fakih, A. Favron, E. Gaufrès, G. Gervais, R. Martel and T. Szkopek, *Nat. Commun.*, 2015, **6**, 7702.
79 N. Gillgren, D. Wickramaratne, Y. Shi, T. Espiritu, J. Yang, J. Hu, J. Wei, X. Liu, Z. Mao, K. Watanabe and T. Taniguchi, *2D Mater.*, 2014, **2**, 011001.
80 X. Li, R. Grassi, S. Li, T. Li, X. Xiong, T. Low and Y. Wu, *Nano Lett.*, 2017, **18**, 26–31.
81 S. D. Sarma and E. H. Hwang, *Solid State Commun.*, 2005, **135**, 579–590.
82 A. Avsar, I. J. Vera-Marun, J. Y. Tan, K. Watanabe, T. Taniguchi, A. H. Castro Neto and B. Ozyilmaz, *ACS Nano*, 2015, **9**, 4138–4145.
83 L. Yu, Y. H. Lee, X. Ling, E. J. Santos, Y. C. Shin, Y. Lin, M. Dubey, E. Kaxiras, J. Kong, H. Wang and T. Palacios, *Nano Lett.*, 2014, **14**, 3055–3063.
84 Y. Liu, H. Wu, H. C. Cheng, S. Yang, E. Zhu, Q. He, M. Ding, D. Li, J. Guo, N. O. Weiss and Y. Huang, *Nano Lett.*, 2015, **15**, 3030–3034.

This journal is © The Royal Society of Chemistry 2019